Crustal Structure of Southern California from Velocity and Attenuation Tomography

Thomas H. Jordan*

Department of Earth Sciences, University of Southern California, Los Angeles, CA 90089

Article history: received September 4, 2024; accepted September 26, 2024

Abstract

Recent studies of Southern California have employed velocity and attenuation tomography to elucidate two aspects of crustal structure. Low-frequency velocity tomography reveals large-scale heterogeneity that can be approximated by a discrete set $(K \le 10)$ of tectonic regions, each characterized by an isostatically balanced lithospheric column reflecting the composition and tectonic history of the region. The boundaries between tectonic regions are typically localized structures expressed at the surface by major faults, topographic fronts, and geochemical transitions. The efficacy with which tomographic regionalization (TR) represents the subsurface geography of major tectonic units in Southern California indicates that the TR idealization works surprisingly well in this part of the Pacific-North America plate boundary. High-frequency attenuation tomography in Southern California supports the hypothesis that the decay of P and S waves propagating through the upper and middle crust is dominated by elastic scattering from small-scale heterogeneities of high fractal dimension, rather than by anelastic dissipation. The amplitude of the scattering varies systematically among the tectonic regions and correlates with the degree of recent faulting and deformation within a region. These results motivate speculation that small-scale crustal heterogeneities responsible for high-frequency attenuation are generated within the seismogenic zone through a dynamic interplay between distributed deformation and localized fracturing.

Keywords: Crust; Tomography; Attenuation; Scattering; Tectonics; Southern California

1. Introduction

Southern California spans one of the world's most seismically active continental plate boundaries and has served the geosciences as a well-monitored natural laboratory for the system-level study of earthquake activity and tectonic deformation. The broadband digital recording of earthquakes by the Southern California Seismic Network (SCSN) began with the TERRAscope initiative in the 1980's and greatly expanded with the deployment of TriNet in the late 1990's (Hauksson et al., 2001). These rich datasets have allowed seismologists to devise structural models that can explain the spatial and frequency dependence of wave propagation and attenuation across the region. Among the methods developed for this purpose are tomographic techniques for imaging the three-dimensional (3D) velocity and attenuation structure of the Southern California crust (e.g., Hauksson, 2000; Schlotterbeck and Abers, 2001; Hauksson and Shearer, 2006; Chen et al., 2007b; Lin et al., 2010; Tape et al., 2010; Lee et al., 2014a; Lin and Jordan, 2023).

This presentation concerns what we have learned about Southern California crust from the velocity and attenuation tomography. My topics will be two types of structural heterogeneity: large-scale lateral variations with characteristic widths much greater than the crustal thickness (\sim 30 km), and small-scale heterogeneities with characteristic dimensions much less than the crustal thickness. The literature on these topics is huge, and I will not attempt a comprehensive review. Instead, I will focus on the results from four recent studies: the low-frequency (\leq 0.2 Hz) velocity tomography of Lee et al. (2014a), which produced the high-resolution CVM-S4.26 model; the *K*-means cluster analysis of CVM-S4.26 velocity profiles by Eymold and Jordan (2019, abbreviated EJ19), which partitioned Southern California into a discrete set of tectonic regions; and the high-frequency (1-10 Hz) attenuation tomography of Lin and Jordan (2018, 2023, abbreviated LJ18 and LJ23), which highlighted the role of scattering by small-scale heterogeneities. The figures in this article, and many of the key points, are drawn from those original reports.

My purpose is to evaluate the observational support for two basic hypotheses about crustal structure. The first comes from the EJ19 regionalization of the velocity tomography, described in Section 2:

H1. The large-scale heterogeneity of Southern California can be approximated by a discrete set of tectonic regions, each characterized by an isostatically balanced lithospheric column that reflects the composition and tectonic history of the region. The boundaries between tectonic regions are typically localized structures expressed at the surface by major faults, topographic fronts, and geochemical transitions.

The second hypothesis is derived from the LJ18 and LJ23 studies of attenuation structure, summarized in Section 3: H2. The attenuation of high-frequency *P* and *S* phases propagating through the upper and middle crust is dominated by elastic scattering from small-scale heterogeneities of high fractal dimension, rather than by anelastic dissipation. The amplitude of the scattering varies systematically among the tectonic regions and correlates with the rate of faulting and deformation within a tectonic region.

The positive correlation of small-scale velocity variability with large-scale deformation motivates the speculation in Section 4 that the small-scale crustal heterogeneities responsible for high-frequency attenuation are generated within the seismogenic zone through a dynamic interplay between distributed deformation and localized fracturing.

2. Low-frequency velocity tomography

A variety of seismic velocity models have been derived using earthquake and ambient-noise data recorded by the SCSN and auxiliary stations deployed temporarily within Southern California (Hauksson, 2000; Chen et al., 2007b; Lin et al., 2010; Tape et al., 2010; Allam & Ben-Zion, 2012; Lee et al., 2014a; Zigone et al., 2015; Ajala et al., 2019; Fang et al., 2022). My discussion will focus on the results of Lee et al. (2014a), who estimated *P* and *S* velocities of the crust and upper mantle across the entirety of Southern California using full-3D tomography (F3DT).

2.1 CVM-S4.26 tomographic model

In F3DT, the starting model is three-dimensional (3D), and both the forward wavefield simulations and the sensitivity kernels are calculated using the full physics of 3D wave propagation; no high-frequency approximations are made (Zhao et al., 2005; Tromp et al., 2005; Chen et al., 2007a,b; Tape et al., 2010). In a major project to improve the Community Velocity Model (CVM) of the Southern California Earthquake Center (SCEC), Lee et al. (2014a) applied 26 iterates of this technique to fit 550,000 low-frequency ($f \le 0.2$ Hz) differential waveform measurements from 38,000 seismograms and 12,000 ambient-noise correlagrams. The final iterate, CVM-S4.26, produced isotropic velocity profiles at 1.52 million geographic nodes spaced at 500-m intervals. At the n^{th} geographic node \mathbf{x}_n , the P-wave and S-wave velocity profiles, $V_P(\mathbf{x}_n, z)$ and $V_S(\mathbf{x}_n, z)$, are discretized at 500 m depth intervals from the surface at z=0 to a depth of $z_{\text{max}}=49.5$ km. Map slices and cross-sections of the CVM-S4.26 model can be found in the original Lee et al. (2014a) paper, as well as in EJ19.

A number of studies have validated the quality of CVM-S4.26 by retrospective and prospective testing. The model captures many crustal features previously identified by surface mapping, borehole data, sonic logs, and active-source imaging, including the geometry of major sedimentary basins (Lee et al., 2014a,b; Lee and Chen, 2016)

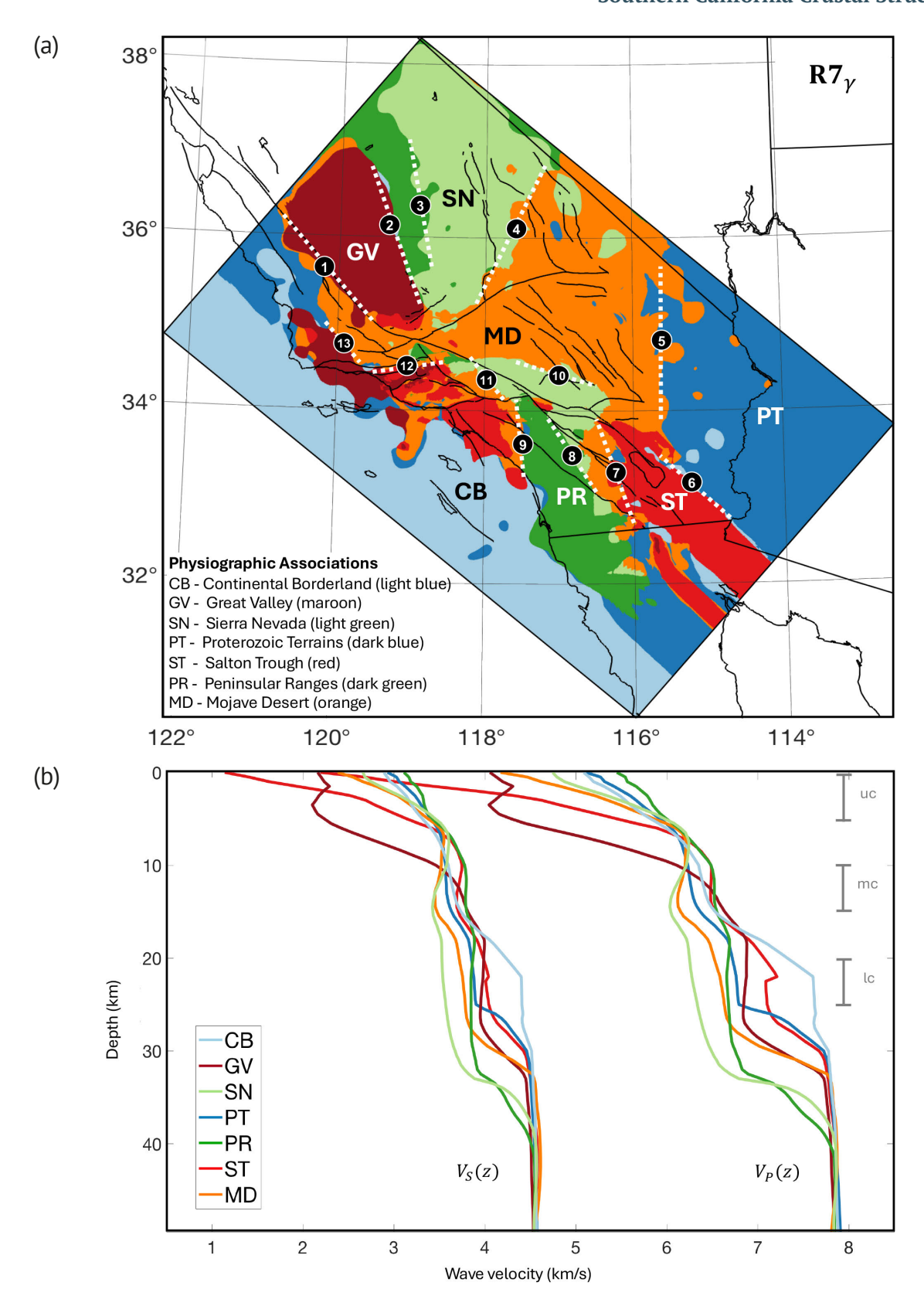


Figure 1. $R7_{\gamma}$ regionalization derived by EJ19 from a K-means cluster analysis of the CVM-S4.26 tomographic model in which K was fixed at 7 and the V_P and V_S profiles were equally weighted. (a) Map of Southern California showing the seven clusters as colored regions labeled by their associated physiographic provinces (Table 1). Dashed white lines are the regional boundaries L1-L13 described in Table 2. (b) Centroid velocity profiles for the $R7_{\gamma}$ regions. Colors and labels are the same as in (a). Gray bars show depth intervals used to compute the upper-crustal (uc), middle-crustal (mc), and lower-crustal (lc) profile averages for the isostatic modeling of Fig. 2. (Source: EJ19, Figs. 7 and 8).

and the localized contrasts across faults that juxtapose crustal blocks of different compositions and tectonic histories (Lee and Chen, 2017). CVM-S4.26 also shows good skill in predicting the low-frequency waveforms observed for earthquakes not included in the inversion dataset, out-performing other models in head-to-head tests (Lee et al., 2014b; Taborda et al., 2016; Lee & Chen, 2016; Lu and Ben-Zion, 2022).

2.2 Tomographic regionalization

Eymold and Jordan (EJ19) applied the K-means++ cluster-analysis algorithm of Arthur and Vassilvitskii (2007) to condense the lateral variation of CVM-S4.26 into a small set ($K \le 10$) of geographically coherent regions. The cluster analysis employed an iterative process to partition the 1.52 million V_P - V_S profile pairs into K groups whose cluster-averaged (centroid) profiles minimized the total inter-cluster variance of the CVM-S4.26 profile set. The K = 7 regionalization, considered to be the most informative (Fig. 1), reduced the inter-cluster variance of the profile set by about 61% relative to the K = 1 profile mean. This tomographic regionalization is denoted $R7_\gamma$, where the subscript γ indicates that the V_P and V_S profiles were equally weighted in the cluster analysis.

The regionalization procedure of EJ19 was well behaved. The cluster analyses for $K \le 10$ generated a coherent sequence of structural refinements: each increment of K introduced a new region, typically by partitioning a larger region into two smaller regions or by occupying a transition zone between two regions. An extensive series of sensitivity tests found that the regionalizations were quite robust. The final regional configurations did not depend on the seed of the cluster initialization, verifying that the algorithm converged to the global minima of the total inter-cluster variance. The regionalizations were insensitive to the weighting of V_P relative to V_S ; e.g., for $K \le 7$, those based only on V_P were very similar to those based only on V_S . To further test the robustness of $R7_{\gamma}$, we trimmed CVM-S4.26 by excluding the outer 50 km of the model domain, which reduced the total model area by 30% and eliminated most areas of poor tomographic resolution that could potentially bias the cluster analysis. The K = 7 regionalization obtained for the trimmed and untrimmed models were nearly identical (see EJ19, Fig. S2).

2.3 Correlation of tomographic regions with surface features

The preferred regionalization, $R7_{\gamma}$, is given by a geographic map of the seven disjunct regions (Fig. 1a) and the average P and S profiles for each region, $V_P^{(k)}(z)$ and $V_S^{(k)}(z)$ (Fig. 1b). All seven regions can be associated with one

Region	Area (km²)	Main Province	Other Tectonic Units	
СВ	79,242	Continental Borderland	none	
GV	29,857	Great Valley	Santa Maria & Santa Barbara Basins	
SN	51,767	Sierra Nevada	Central Transverse Ranges	
PT	82,807	Proterozoic Terranes	none	
PR	31,505	Peninsular Ranges	Western Sierra Nevada	
ST	29,546	Salton Trough	Los Angeles & Ventura Basins	
MD	76,204	Mojave Desert	Western Transverse & Southern Coast Ranges	

Table 1. Association of $R7_{\gamma}$ regions with Southern California physiographic provinces and tectonic units.

Southern California Crustal Structure

or more physiographic provinces and tectonic units (Table 1). Many of the boundaries between regions are lineated features that align with major faults, topographic fronts, and geochemical transitions mapped at the surface. The thirteen structural lineations L1-L13 used by EJ19 to test the tomographic/tectonic correspondence are listed with references in Table 2 and shown as dashed white lines in Fig. 1a.

A region is labeled with the two-letter abbreviation of its main associated province; e.g., the dark green region of Fig. 1a is associated with the Peninsular Ranges (PR), and the light green region with the Sierra Nevada (SN). Both batholithic regions are characterized by thickened crust columns with mean M-discontinuity (Moho) depths of $z_{\rm M}=36.5$ and 35.0 km, respectively. However, the average shear velocities of the PR region are about 0.3 km/s higher throughout the crust, consistent with the Peninsular Range batholith having a more mafic composition (Christensen and Mooney, 1995).

Part of the PR region occupies in the western Sierra Nevada, while parts of the SN region are found in the central Transverse Ranges and along the eastern side of the Peninsular Ranges. This distribution matches a well-documented compositional dichotomy of the Cretaceous California Arc, which geologists and geochemists divide into an older (ca. 140-100 Ma) western zone of tonalitic/gabbroic plutons with oceanic affinities and a younger (ca. 100-80 Ma) eastern zone of granitic/granodioritic plutons with continental affinities (Chapman et al., 2012, 2016; Jiang & Lee, 2017).

Line number*	Structural identification	Region pair	References			
L1	San Andreas fault, Parkfield to Carrizo	MD-GV	Shaw et al., 2015			
L2	Kings-Kaweah ophiolite boundary	GV-PR	Saleeby, 2011; Godfrey & Klemperer, 1998			
L3	Sierra Nevada west-east plutonic boundary, Sr-706 line	PR-SN	Chapman et al., 2012; Kistler & Peterman, 1978			
L4	Crustal thickening front, Early Permian continental margin	SN-MD	Stevens & Stone, 2005; Kucks, 1999			
L5	Eastern Mojave LIL enrichment transition, 116° line	MD-PT	Miller et al., 2000; Luffi et al., 2009			
L6	Algodones-Altar fault system, Pliocene plate boundary	PT-ST	Beard et al., 2016; Howard et al., 2015			
L7	Western Salton detachment fault	ST-MD	Mason et al., 2017			
L8	Peninsular Range Batholith boundary	SN-PR	Jiang & Lee, 2017; Langenheim et al., 2004			
L9	San Gabriel-Chino Hills-Cristianitos fault system	PR-MD	Ehlig, 1979; Klotsko et al., 2015			
L10	North frontal thrust of Big Bear Block	SN-MD	Yan & Clayton, 2007; Spotila & Sieh, 2000			
L11	Vincent fault	MD-SN	Fuis et al., 2001			
L12	San Cayetano-Ventura-Pitas Point fault system	ST-MD	Hubbard et al., 2014; Marshall et al., 2017			
L13	Nacimiento fault	GV-MD	Chapman et al., 2016			
* Line numbers identify white dashed lines in Fig. 1a.						

Table 2. Selected region boundaries delineated by the $R7_{\nu}$ cluster analysis.

In the Sierra Nevada, geochemists have used the "0.706 line" in the initial strontium ratios (87 Sr/ 86 Sr) $_i$ to separate the western and eastern plutonic zones (Kistler & Peterman, 1978; Chapman et al., 2012). The PR-SN boundary, marked L3 in Fig. 1a, is a good match to the 0.706 line (EJ19, Fig. 15a). In the Peninsula Ranges, the PR-SN boundary, marked L8, accurately separates the petrologically distinct western-zone plutons from those of the eastern-zone, as mapped by Jiang & Lee (2017). This line also traces the "Peninsular Range Batholith boundary" detected by Langenheim et al. (2004) using gravimetric and magnetic data.

A variety of regional associations and structural correlations have been documented in EJ19. Among the more salient are the following five:

- a) Eight of the thirteen lineated boundaries correspond to major faults. Three are currently active San Andreas (L1), North Frontal Thrust (L10), and San Cayetano-Ventura-Pitas Point (L12). The other five Algodones-Altar (L6), Western Salton Detachment (L7), Cristianitos (L9), Vincent (L11), and Nacimiento (L13) are now quiescent but played important roles in the Cenozoic tectonic assembly of Southern California (see references in Table 2).
- b) The large sedimentary basins in Southern California are captured in two regions: GV, associated with the Great Valley, and ST, associated with the Salton Trough. The latter differs from the former by having a higher-velocity middle and lower crust and a shallower M-discontinuity, consistent with a mean ST crustal column that is thinner and more mafic than its GV counterpart. The Santa Maria Basin, which contains sediments of the Great Valley Group and, like the Great Valley, is underlain by Franciscan basement (Chapman et al., 2016), plausibly associates with GV, whereas the Los Angeles basin, which is underlain by higher-velocity basement (Godfrey et al., 2002), associates primarily with ST.
- c) The two regions associated with the Mojave Desert (MD) and the Proterozoic Terranes (PT) of eastern California and western Arizona are contiguous and structurally similar (Condie, 1982). The PT region has higher velocities in the middle and lower crust than MD, and its M-discontinuity is shallower, which can be explained if the PT crustal column is thinner and has a more mafic composition. The MD-PT boundary in the eastern Mojave Desert (L5) runs approximately north-south along 115.6°W (Fig. 1a). This longitude is close to the "116° line" identified by Miller et al. (2000) from the geochemical signatures of Miocene basalts. Basalts east of 116°W indicate an ancient (Proterozoic) lithospheric source enriched in large-ion lithophile (LIL) elements, whereas no basalts with enriched-lithosphere signatures have been found west of this longitude. According to Luffi et al. (2009), "a major compositional boundary lies within the midcrust to deep crust of the central Mojave, demarcating a western domain containing abundant schist as basement rocks and an eastern domain lacking significant schist and containing significant remnants of old continental lithosphere."
- d) One of the more cryptic regional boundaries is L4, which separates thicker SN crust from thinner MD crust along an irregular topographic front that cross-cuts the Death Valley/Panamint Valley extensional domain at a high angle to the SSE-NNW axis of the late-Cenozoic pull-apart basins. This boundary coincides with a strong Bouguer gravity gradient (Kucks, 1999) and aligns with a northeast-trending segment of the Early Permian continental margin (Stevens & Stone, 2005).
- e) The CB region associates with the attenuated, submerged crust of the offshore California Continental Borderlands and has no significant onshore component.

As these examples demonstrate, the regionalization results are coherent with a wide range of information about tectonic structure of Southern California. The geographic correlations are remarkable because the tomographic inversions and cluster analyses contained no direct information about the regional physiography or geology. The conformance of the tomographic regionalization with surface mapping thus provides strong evidence for the tectonic significance of the major features in Fig. 1.

Moreover, the close spatial correlation of the deep-seated tomographic region boundaries with surface-mapped structures indicates that many of those boundaries are localized structures with lateral widths on the order of a crustal thickness or less. One exception may be the MD-PT boundary in the eastern Mojave Desert (L5), which may mark a wider transition (EJ19). Overall, however, the transition widths are relatively small compared to the region size.

2.4 Isostasy of the tomographic regions

The requirement of isostatic equilibrium places integral constraints on models of lithospheric structure (e.g., Romanyuk et al., 2007; Schmandt et al., 2015), but no such constraints were applied in the construction of

CVM-S4.26. Therefore, the degree to which the $R7_{\gamma}$ regions are in isostatic balance provides another posterior check on the tectonic plausibility of the tomographic regionalization. It also yields new information about how isostasy is actually achieved.

In EJ19, we demonstrated that the $R7_{\gamma}$ regions are in approximate isostatic equilibrium using the simplified isostatic model depicted in Fig. 2a. P-wave velocities were converted to densities using Brocher's (2005) relationship, and density anomalies relative to the model mean were estimated for the three crustal layers of the k^{th} region, $\{\Delta\rho_{\text{lc}}^{(k)}, \Delta\rho_{\text{lc}}^{(k)}\}$, from V_P averages taken over the depth intervals 0-5 km, 10-15 km, and 20-25 km (Fig. 1b). Areal mass anomalies $\{\Delta M_{\text{uc}}^{(k)}, \Delta M_{\text{mc}}^{(k)}, \Delta M_{\text{lc}}^{(k)}\}$ were computed by multiplying the density anomalies by the layer thicknesses, assuming $\bar{z}_{\text{uc}} = 6$ km and $\bar{z}_{\text{mc}} = 16$ km. The uc and lc mass anomalies were augmented to account for the regional variations in elevation $h^{(k)}$ and the depth of the M discontinuity $z_{\text{M}}^{(k)}$, respectively. We solved for the upper-mantle density anomaly $\Delta\rho_{\text{um}}^{(k)}$ by requiring isostatic balance at a depth of compensation $z_{\text{lith}} = 60$ km, assuming a mean mantle density of $\bar{\rho}_{\text{um}} = 3200$ kg/m³ and a mantle layer thickness of $\Delta z_{\text{um}}^{(k)} = z_{\text{lith}} - z_{\text{M}}^{(k)}$. That balance can be written

$$\left[\frac{\Delta M_{\rm uc}^{(k)} + \Delta M_{\rm mc}^{(k)}}{\Delta z_{\rm um}^{(k)}} \right] + \frac{\Delta M_{\rm lc}^{(k)}}{\Delta z_{\rm um}^{(k)}} + \Delta \rho_{\rm um}^{(k)} = 0$$
 (1)

Figure 2b plots the first term of this equation against the second. On this graph, the upper-mantle density anomalies that satisfy the isostatic condition (Eq. 1) are constant along anti-diagonal lines.

The very strong anticorrelation of the uc+mc anomalies with the lc anomalies (r = -0.96) demonstrates that, to first order, the isostasy is crustal. The regions are dispersed along the antidiagonal of Fig. 2b because large density variations in the upper half of the crust are, for the most part, compensated by variations of the opposite sign in the lower half. This top-to-bottom anticorrelation produces "structural dipoles" with vertical scales comparable to the crustal thickness. Such anomalies are easily resolved by the F3DT inversions, at least in areas where the wave-path coverage is good, which helps to explain the robustness of the regionalization results.

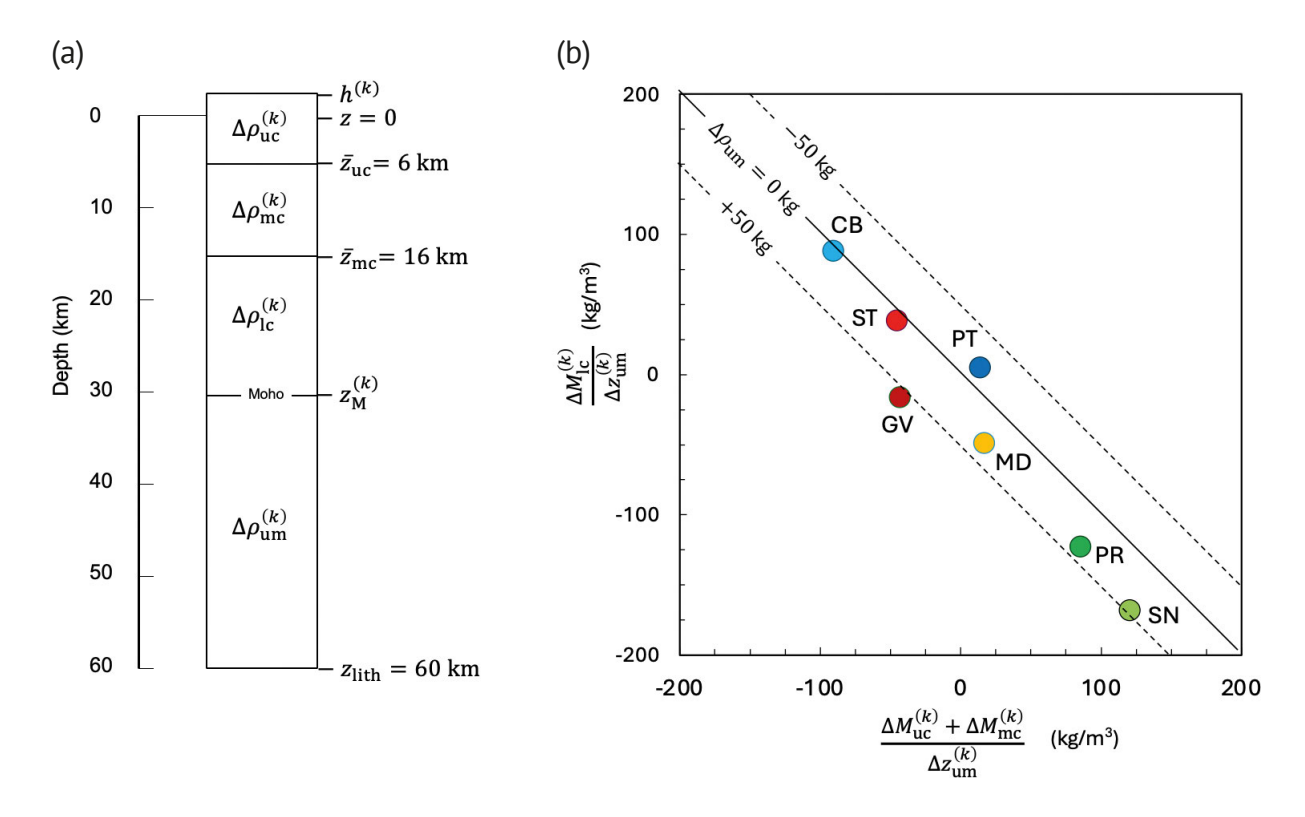


Figure 2. (a) Four-layer isostatic model of EJ19. Quantities superscripted with k are regionally variable. (b) Plot of the lower-crust anomaly against the upper- and mid-crustal anomaly. Colored circles are average values for the $R7_{\gamma}$ regions of Fig. 1 derived from layer-averaged velocities using Brocher's (2005) nonlinear $V_P - \rho$ relationship. Diagonal lines are the contours of the upper-mantle density anomalies that satisfy the isostatic balance of Eq. (1). (Source: EJ19 Fig. 13 recomputed using $\bar{z}_{\rm M} = 30$ km and a corrected CB value).

The upper-mantle density anomalies are small; six of the seven regions fall within the central diagonal band $\Delta \rho_{\rm um}^{(k)} = 0 \pm 50 \, {\rm kg/m^3}$, which is within the range of basaltic enrichment and depletion observed in mantle peridotites (e.g., Jordan, 1979). The regional estimates of $\Delta \rho_{\rm um}^{(k)}$ implied by isostatic balance have high relative uncertainties, but they are consistent in some cases with the gravimetric data and geologic models. For example, the positive anomaly obtained for the SN region (+ 48 kg/m³) agrees with the high upper-mantle densities that Kaban & Mooney (2001) found for the eastern zone of the Sierra Nevada batholith. The mantle density anomaly is also positive for the PR region (+ 37 kg/m³), consistent with a denser "arclogite root" beneath both batholithic regions (Saleeby et al., 2012).

The regional isostatic equilibrium of Fig. 2b, like the consistency of the region boundaries with surface mapping (Fig. 1a), is evidence that $R7_{\gamma}$ approximates true features of large-scale tectonic structure. A case in point concerns the three regions SN, MD, and PT, which taken together, constitute the continental lithospheric domain of Southern California (EJ19). Rocks with the geochemical signatures of continental lithosphere are ubiquitous in these three tomographic regions, but rarely found in the other four. Within this continental domain, the inferred densities of the middle and lower crust increase in the ordered sequence SN \rightarrow MD \rightarrow PT, and the M-discontinuity depths decrease in their proper isostatic proportions (see EJ19, Fig. 12). This ordering, which is also observed in the heat flow (Sass et al., 1994), can be explained by the progressive thinning of orogenically over-thickened crust, accompanied by basaltic intrusion and densification of the lower and middle crust. The regionalized velocity profiles are thus consistent with a viable model of Cenozoic tectonic stretching and magmatism within the southern Basin and Range province (Lachenbruch et al., 1994; Gans and Bohrson, 1998; Parsons, 2006).

3. High-frequency attenuation tomography

Under the assumptions of linear anelasticity, seismic attenuation is described by a dimensionless parameter, the inverse quality factor $Q^{-1} \ll 1$, which measures the fractional energy loss per wave cycle. This attenuation factor is a local property of the crust that varies with wave type (P or S), geographic position \mathbf{x} , depth z, and frequency f. The goal of attenuation tomography is to estimate $Q_P^{-1}(\mathbf{x}, z, f)$ and $Q_S^{-1}(\mathbf{x}, z, f)$.

In a recent study of Southern California attenuation structure, we measured the spectral amplitudes in the high-frequency band (1-10 Hz) from large sets of P and S waveforms of regional earthquakes recorded by SCSN broadband stations (LJ23). Spectral ratios of these direct phases were calculated relative to synthetic seismograms that accounted for source radiation patterns and frequency-dependent propagation through the laterally averaged CVM-S4.26 velocity structure. These data were inverted for 1D and 3D attenuation models within the CVM-S4.23 study region. Completely separate inversions were run for the Q_P^{-1} dataset (290,000 P-wave spectral ratios) and Q_S^{-1} dataset (220,000 S-wave spectral ratios) in 1-Hz intervals from 1 to 10 Hz.

3.1 Frequency dependence and the Q_P^{-1}/Q_S^{-1} ratio

Previous studies of crustal waves have demonstrated that high-frequency attenuation can be approximated as a power law in frequency, $Q^{-1} \sim f^{-\alpha}$, where α is a positive decay exponent that depends on the wave type (Aki, 1980; Atkinson, 1995; Sato et al., 2012). Published estimates of α for Lg propagation in Southern California range from 0.45 to 0.67 (Raoof et al., 1999; Erickson et al., 2004). Significantly higher values ($\alpha_S \approx 1$) have been obtained by the analyses of S-wave coda envelopes (Jin et al., 1994; Eulenfeld and Wegler, 2017).

We constrained the frequency dependence by separately inverting the datasets for the laterally averaged profiles, $\bar{Q}_P^{-1}(z,f)$ and $\bar{Q}_S^{-1}(z,f)$, and then averaging these profiles over the upper and middle crust to obtain the estimates in Fig. 3. Points for the individual frequency bands are well fit by a power law with $\alpha_P=0.30\pm0.03$ and $\alpha_S=0.37\pm0.02$. These decay exponents are nearly equal but significantly lower than the Lg and coda-envelope estimates.

The average P-wave attenuation is 5-20% higher than the average S-wave attenuation across the 1-10 Hz band, in good agreement with Hauksson and Shearer's (2006) 5-Hz model for Southern California, as well as similar results for other continental regions (Sato et al., 2012, Fig. 5.3). The observation $Q_P^{-1}/Q_S^{-1} \gtrsim 1$ excludes the $\sim 4/9$ ratio expected for thermally activated anelasticity dominated by shear dissipation (dashed line in Fig. 3), which is the mechanism most commonly assumed in the modeling of low-frequency seismic attenuation (Knopoff, 1964; Aki and Richards, 2002).

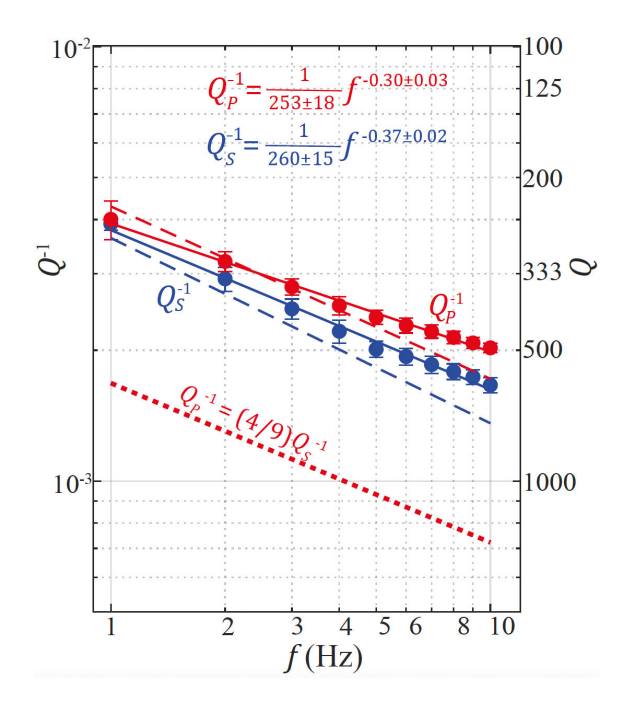


Figure 3. Frequency dependence of attenuation in the Southern California crust in the high-frequency band 1-10 Hz. Red and blue dots with 1-sigma error bars are Q_P^{-1} and Q_S^{-1} values obtained by separate depth-dependent inversions in 1-Hz bands and averaged from the surface to 16 km depth using ray-density weighting. Solid red and blue lines are the least-squares fits; dashed red and blue lines are the results obtained by LJ18. Dotted red line is the Q_P^{-1} calculated from Q_S^{-1} assuming the medium is a Poisson solid and the attenuation is only by shear dissipation (Source: LJ23, Fig. 1b).

This ratio disagreement led Hauksson and Shearer (2006) to invoke partial fluid saturation of crustal rocks, which has been shown in the laboratory and in petroleum reservoirs to be a mechanism for increasing compressional dissipation (Töksoz et al., 1979; Winkler and Nur, 1982). Partial saturation may play a substantial role in the highly attenuating uppermost crust, but it is unlikely to dominate at depths below about 6 km, where the pressures become high enough to close most gas-filled cracks and porosity drops below the percolation threshold (Benson et al., 2006). Our preferred alternative to explain the ratio disagreement is the high-frequency scattering hypothesis, which states that elastic scattering from small-scale crustal heterogeneities, not an elastic dissipation, dominates high-frequency attenuation. The arguments supporting the scattering hypothesis are reviewed in Section 3.3.

3.2 The SCAT model

In the inversion for 3D attenuation structure, LJ23 fixed the decay exponents at the mean values obtained in the 1D analysis (Fig. 3) and expressed the 3D structure as relative perturbations to the mean depth profiles:

$$Q_P^{-1}(\mathbf{x}, z, f) = \overline{Q}_P^{-1}(z, f_0) [1 + \Delta \ln Q_P^{-1}(\mathbf{x}, z, f_0)] \left(\frac{f}{f_0}\right)^{-0.30}$$
(2a)

$$Q_S^{-1}(\mathbf{x}, z, f) = \overline{Q}_S^{-1}(z, f_0) [1 + \Delta \ln Q_S^{-1}(\mathbf{x}, z, f_0)] \left(\frac{f}{f_0}\right)^{-0.37}$$
(2b)

The perturbations $\Delta \ln Q^{-1}$ were discretized on a 20-km square horizontal grid that covered the CVM-S4.26 study area and a 0.5-km vertical grid that extended from the surface to a depth of 49.5 km. The inversion outputs are plotted at the reference frequency $f_0 = 5$ Hz in Fig. 4. The 1D mean profiles and 3D perturbations combined with the frequency dependence of Eq. (2) constitute the Southern California Attenuation Tomography (SCAT) model (LJ23).

The SCAT model features large, geographically coherent attenuation anomalies with variations of up to \pm 50% that extend downward through the upper and middle crust. The Q_P^{-1} and Q_S^{-1} variations are very similar. For the layer averages in Fig. 4, the mean Q_P^{-1}/Q_S^{-1} ratios increase with depth, from 1.07 in the uppermost crust to 1.24 in the lower crust. The Q_P^{-1}/Q_S^{-1} correlations are high, ranging from $r \approx 0.8$ in the upper and middle crust to about 0.6 in the lower crust. As in the 1D case, the P and S inversions were conducted separately, so that the good agreement observed between the two independent perturbations constitutes what statisticians call a "severe test" of the model (Mayo, 2018): it is highly unlikely that recovered values of the P and S attenuation factors would be so strongly correlated if their actual values were not strongly correlated.

Because the Q_S^{-1} and Q_S^{-1} structures are so similar in the upper 16 km, we combined them into a 2D mean attenuation anomaly,

$$\Delta \ln Q_{\text{avg}}^{-1}(\mathbf{x}) = \frac{1}{2} [\Delta \ln Q_P^{-1}(\mathbf{x}) + \Delta \ln Q_S^{-1}(\mathbf{x})]$$
 (3)

Each of the two terms is obtained by ray-path weighted averaging of the relative perturbations from the surface to 16 km depth. The results are plotted in Fig. 5. The dashed black line encompasses the high-resolution area where the anomaly amplitudes are larger than those in the low-resolution periphery. The solid black lines delineate a regionalization of the high-resolution area adapted from $R7_{\gamma}$. For this comparison, LJ23 simplified the regional boundaries, excluded three of the regions poorly sampled by the attenuation data (GV, PT, CB), and added a new LA region, which in $R7_{\gamma}$ is a heterogeneous mixture of the ST and MD regions.

The large-scale geographic pattern of the anomalies in Fig. 5 is similar to that imaged in previous tomographic studies (e.g., Hauksson and Shearer, 2006; Phillips and Stead, 2008; Hearn, 2020). Negative (blue) anomalies are largely confined to the Mesozoic batholiths of the PR and SN regions, whereas positive anomalies (red) are restricted to the MD, ST, and LA regions. Exceptions are the central and eastern parts of MD, which show negative to neutral anomalies. In the northern and western parts of MD, a positive anomaly associated with the Garlock and White Wolf fault systems separates the two SN components of the batholithic belt. To the northeast, the Garlock anomaly connects with the positive anomalies of the Walker Lane and Eastern California Shear Zone. To the west, it extends

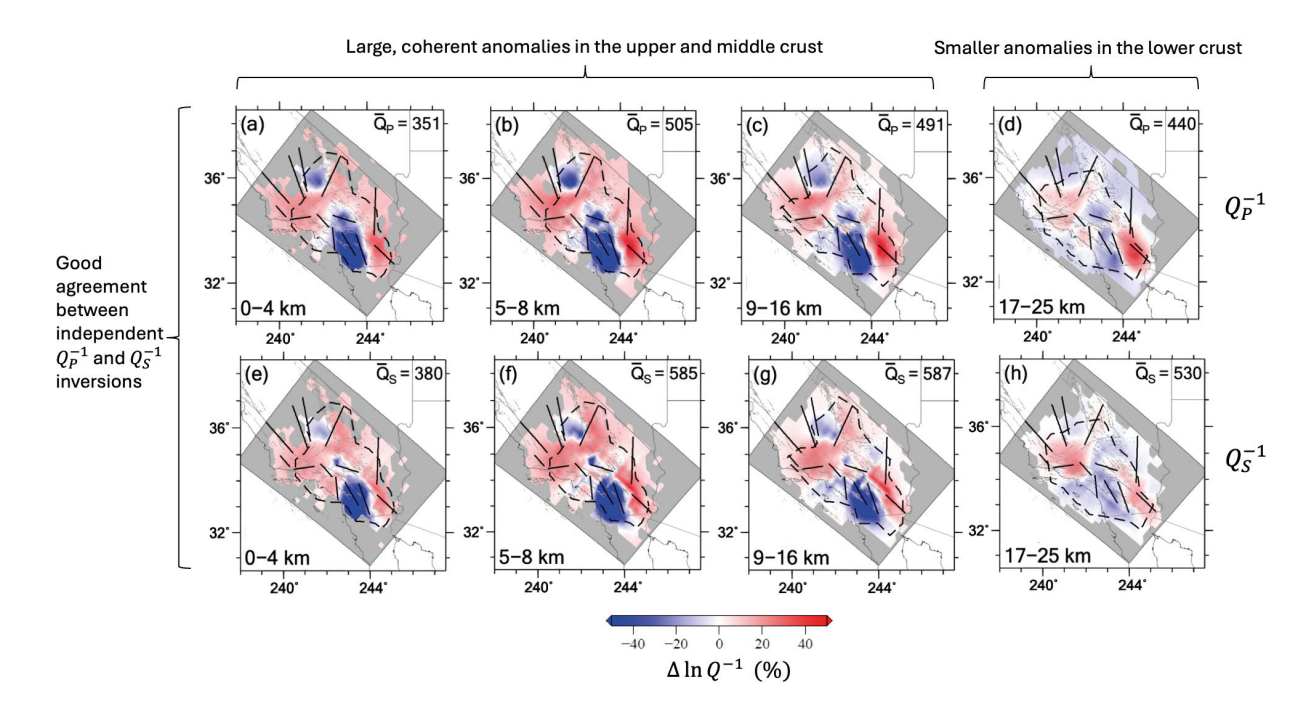


Figure 4. Map views of the SCAT model at $f_0 = 5$ Hz showing relative perturbations $\Delta \ln Q_P^{-1}$ (a-d) and $\Delta \ln Q_S^{-1}$ (e-h) averaged over the depth ranges 0-4 km (left column), 5-8 km, 8-16 km, and 17-25 km (right column). Color scale ranges from -50% (deep blue) to +50% (bright red). The quality factors \bar{Q} annotated in each panel are inverses of the layer-averaged attenuation factors. Dashed black lines enclose the model volume where the resolving power of the inversion is relatively high. Light gray lines are traces of major faults (Source: LJ23, Fig. 3).

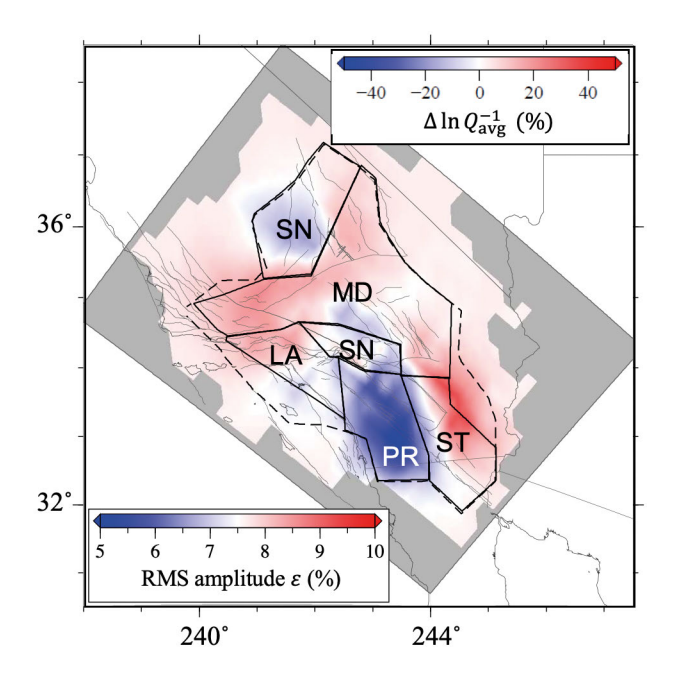


Figure 5. Map of the 2D mean attenuation anomaly $\Delta \ln Q_{\rm avg}^{-1}(\mathbf{x})$ obtained by averaging the P and S models from the surface to 16 km depth using a ray-density weighting. Scale of the relative perturbation is shown in the upper right. Scale in the lower left gives the RMS relative amplitude $\varepsilon(\mathbf{x})$ needed to reproduce the attenuation anomaly if the other parameters of the Sato-Fehler scattering model are held constant at the values described in the text. The mean RMS relative amplitude is $\varepsilon_0 = 7.5\%$ (white), and the lateral variations range from 4.6% (deep blue) to 9.2% (bright red). Dashed black line encloses the area where the resolving power of the inversion is relatively high. Solid black lines delineate the modified regionalization adapted by LJ23 from the $R7_{\gamma}$ regionalization of Fig. 1a, which was confined to the high-resolution area. Two-letter region labels are the same as in Table 1, except for the addition of an LA region. Light gray lines are active faults (Source: LJ23, Fig. 7c).

into a broad anomaly centered on the San Andreas/Garlock triple junction of the western Transverse Ranges. The attenuation also increases where the San Andreas fault system crosses the batholithic belt at the San Gorgonio Pass, but here the anomaly is only less negative (whiter) rather than positive, perhaps because the San Andreas zone of deformation is narrower where it crosses the batholiths and thus more poorly resolved by the tomography.

The anomalies in the lower crust (below 16 km) correlate well with the shallower structure, but they are generally smaller in amplitude (Fig. 4). Computational experiments to assess the resolving power of synthetic datasets indicated that the tomographic inversions smear shallow anomalies into the lower crust (see LJ23, Figs. 9S-14S). Consequently, the amplitudes of the lower crustal anomalies in the SCAT model may biased to higher values than they actually are.

From the 3D anomaly distribution of the SCAT model, we can draw two inferences: (1) the physical processes that govern attenuation have produced higher attenuation factors in regions of active faulting and deformation and lower attenuation factors in the relatively undeformed batholithic regions, and (2) these processes have generated lateral variations in the upper and middle crust that are larger than those in the lower crust. The spatial dependencies thus suggest a relationship between attenuation and seismogenesis.

3.3 The High-Frequency Scattering Hypothesis

The amplitude reduction of seismic waves with propagation distance can be modeled as the combined effect of two mechanisms: intrinsic dissipation, in which seismic energy is converted to heat by anelastic processes, and elastic scattering, in which seismic energy is dispersed from the waveform by elastic interactions within the heterogeneous crust (Sato et al., 2012). Assuming the two processes are independent, the total fractional energy loss per wave cycle is simply the sum of the two attenuation factors, $Q^{-1} = {}^{In}Q^{-1} + {}^{Sc}Q^{-1}$. The relative importance of the two mechanisms is measured by the seismic albedo, defined to be the scattering fraction of the total attenuation,

 $B = {}^{Sc}Q^{-1}/({}^{In}Q^{-1} + {}^{Sc}Q^{-1})$. The high-frequency scattering hypothesis asserts that ${}^{Sc}Q^{-1} > {}^{In}Q^{-1}$ in the 1-10 Hz band; i.e., B > 0.5.

Sato et al. (2012) summarized the extensive research on the role of scattering in seismic attenuation, and they reviewed the methods for separating ${}^{SC}Q^{-1}$ from ${}^{In}Q^{-1}$ by analyzing the temporal and spatial decay of S-coda envelopes. In Southern California, the application of these methods has found that the S-wave albedo B_S is frequency dependent, ranging from 0.5 at 1 Hz to less than 0.2 at 10 Hz (Frankel, 1991; Jin et al., 1994; Eulenfeld and Wegler, 2017). Wang and Shearer (2017) used Monte Carlo simulations of P and S multiple scattering within the coda to obtain $B \approx 0.3$ at 3 Hz, consistent with the frequency-dependent estimates.

These *S*-coda analyses are in clear contradiction with the high-frequency scattering hypothesis. However, the coda results also disagree with the well-constrained magnitude and frequency dependence of the spatially average *S*-wave attenuation factor shown in Fig. 3. For instance, the 1-Hz value of Q_s^{-1} from Eulenfeld and Wegler's (2017) reference model for Southern California is 1/59, more than a factor of four larger than our average value of $1/(260 \pm 15)$, and their modeling gives a decay exponent of $\alpha_S \approx 1.0$, which is three times larger than the LJ23 estimate of 0.37 ± 0.02 . The reason for the disagreement remains unclear. Our Q_s^{-1} averages appear to be robust; e.g., the values in our first study are statistically indistinguishable from those determined from the much larger dataset in our second (Fig. 3).

In any case, there are several reasons to favor scattering as the dominant attenuation mechanism. One is its physical plausibility. Scattering models with just a few parameters nicely explain the salient aspects of the SCAT model. The particular formulation we have used is the Sato-Fehler scattering model, which gives analytical expressions for ${}^{SC}Q_P^{-1}$ and ${}^{SC}Q_S^{-1}$ as a function of wavenumber k (Sato et al., 2012). These expressions are derived by applying a first-order, fully elastic Born approximation to the scattering of P and S waves from an isotropic distribution of elastic heterogeneities. The elastic medium is a realization of a zero-mean Gaussian random field described by a generalized von Kármán autocovariance function with three parameters: a root-mean-square (RMS) relative amplitude ε , a characteristic outer scale a, and Hurst exponent ν . The fourth parameter is the cutoff scattering angle ψ_c , which removes the forward-scattered (non-attenuating) component from the first-order wavefield. For fixed values of the medium parameters, ψ_c is determined by the ${}^{SC}Q_P^{-1}/{}^{SC}Q_S^{-1}$ ratio.

We have employed the Sato-Fehler model to fit the spatially averaged attenuation spectra at high frequencies (LJ18) and to represent the scattering component of the broadband attenuation model for Southern California (LJ23). The latter, which is shown by the dotted lines in Fig. 6, has the parameters,

$$\varepsilon_0 = 0.075, \ a = 8 \text{ km}, \ \nu = 0.15, \ \psi_c = 40^{\circ}$$
 (4)

The ${}^{Sc}Q^{-1}$ spectra are peaked at $k_{\rm peak}=2\pi/a$ and roll off at higher and lower wavenumbers (Sato et al., 2012). For $k\gg k_{\rm peak}$, scattering attenuation follows a power law that relates the attenuation to the medium parameters,

$${}^{Sc}Q^{-1}(k) \sim \varepsilon^2 (ak)^{-2\nu} \tag{5}$$

With this background, we review a series of six arguments that support of the high-frequency scattering hypothesis:

- 1) On average, the P-wave attenuation factors are greater than or nearly equal to the S-wave attenuation factors across the high-frequency band (Fig. 3) and throughout the crust (Fig. 4). This relationship excludes shear-dominated anelastic models that require $Q_P^{-1}/Q_S^{-1} \approx 4/9$. Based on an assessment of the alternatives, Hauksson and Shearer (2006) advocated partial fluid saturation as the mechanism for increasing the compressional dissipation. As noted above, however, this process can only operate at pressures low enough to allow an interconnected network of partially gas-filled cracks, which limits its domain of viability to the upper crust.
- 2) P and S attenuation factors are nearly equal when they are expressed as a function of wavenumber k (LJ18, Fig. 11). Under the scattering hypothesis, equal attenuation implies that the transport mean free path ${}^{Sc}Q(k)/k$ is the same for P waves and S waves. In the Sato-Fehler model, ${}^{Sc}Q_S^{-1}/{}^{Sc}Q_S^{-1}$ is sensitive to the cutoff scattering angle. This ratio is pegged at unity when $\psi_c \approx 40^\circ$ (LJ18, Fig. 12), which is lies near the middle of the range bounded by causality considerations (Kawahara, 2002).

- 3) Another signature of scattering is the near equality of α_P and α_S . According to Eq. (5), $\alpha=2\nu$, so that these decay parameters should be equal if the roll-offs of the V_P and V_S wavenumber spectra, measured by the Hurst exponent, are the same, i.e., if they have the same fractal (Hausdorff) dimension $D=4-\nu$. Equal roll-offs are expected for velocity heterogeneity, owing to the relatively weak variations of Poisson's ratio in crustal rocks (Brocher, 2005; Lee et al., 2014a). The estimates of the decay exponent, $\alpha\approx0.3$, imply a high fractal dimension, $D\approx3.85$. This inference agrees with the high values ($D\approx3.70$ -3.95) extracted from sonic and resistivity logs (Dolan et al., 1998; Savran and Olsen, 2016) and seismic data (Pullammanappallil et al., 1997; Nakata and Beroza, 2015). If the decay exponents were near unity, as found in the S-coda studies, the implied fractal dimension would be significantly lower ($D\approx3.50$).
- 4) The 3D variations in attenuation do not correlate significantly with thermal variations. Hauksson and Shearer (2006) noted the lack of a relationship with surface heat flow, and (LJ23, Fig. 6) documented the poor correlation with mid-crustal temperatures. An exception is the lower crust of the magmatically active Salton Trough, where Q_P^{-1} is anomalously high. The insensitivity of Q^{-1} to temperature variations indicates that the 3D variations in Southern California are not, in the main, governed by thermally activated anelastic processes.
- 5) The scattering hypothesis implies that the attenuation variations are controlled by the distribution of small-scale velocity heterogeneity. According to Eq. (5), Q^{-1} increases in proportion to the mean squared amplitude of small-scale velocity heterogeneity. The data of Fig. 3 give a spatially averaged RMS amplitude of $\varepsilon_0 = 7.5\%$. If the other Sato-Fehler parameters are held at the mean values given by (4), then the map of $\Delta \ln Q_{\rm avg}^{-1}(\mathbf{x})$ can be rescaled to relative a velocity variation $\varepsilon(\mathbf{x})$, as shown in Fig. 5. Only a modest reduction of ε from 7.5% to 5% is needed to explain the low attenuations imaged in the SN and PR regions, and an increase of similar size, from 7.5% to 10%, can account for the higher attenuation in the ST and MD regions. Small-scale velocity heterogeneities with amplitudes of 5-10% are within the range observed in the seismic and well-log data from Southern California (Süss and Shaw, 2003; Nakata & Beroza, 2015; Savran & Olsen, 2016).
- 6) The SCAT model shows lower attenuation ($\Delta \ln Q_{\rm avg}^{-1} < 0$) in batholiths of Southern California and higher attenuation ($\Delta \ln Q_{\rm avg}^{-1} > 0$) in zones of active faulting (Fig. 5). The scattering hypothesis implies that the former regions should be more homogeneous, whereas the latter should be more heterogeneous. Large batholiths are known to be relatively homogeneous rock masses with low attenuation and low reflectivity (Nelson et al., 1986; Scheirer and Hobbs, 1990). Previous attenuation studies have noted higher scattering in zones of more active faulting, which has been attributed to an increase in small-scale heterogeneity generated by faulting and other deformation processes (Jin et al., 1994; Pei and Chen, 2010; Hearn, 2020).

In the SCAT model, the lateral attenuation anomalies have higher amplitudes in the upper and middle crust than in the lower crust (Fig. 4). Correcting for the bias due to tomographic smearing into the lower crust further suppresses the lower-crustal anomalies. Therefore, the LJ23 results support the notion that the lateral variations of Q_P^{-1} and Q_S^{-1} are primarily due to variability in the RMS amplitude of small-scale velocity heterogeneity in the seismogenic layer (Fig. 5).

3.4 Broadband attenuation model

Although the main features of the high-frequency attenuation can be explained by a Sato-Fehler scattering model with reasonable parameters, intrinsic attenuation must surely play a role, especially at the lower frequencies where the scattering by velocity heterogeneities is expected to be weaker. Low-frequency attenuation is difficult to measure over short paths limited to Southern California, so the uncertainties of the estimates are rather high. Ground-motion simulations up to 0.5 Hz have indicated that attenuation scales nearly linearly with shear velocity, particularly in the low-velocity, high-attenuation sedimentary basins of the upper crust (Olsen et al., 2003; Graves et al., 2008). At typical basement velocities, the low-frequency simulations show an average Q_S^{-1} ranging from about 1/360 to 1/180, assuming the mechanism is anelastic with $Q_P^{-1} = 1/2 Q_S^{-1}$. Hu et al. (2022) used broadband simulations (0-5 Hz) that accounted for source complexity and scattering from the topographic surface to test a variety of frequency- and velocity-dependent anelastic models against data from the 2014 La Habra earthquake. At f = 0.3 Hz and $V_S = 3.6$ km/s, four of their representative Q_S^{-1} models span a range of 1/360-1/87 and have a geometric mean of 1/174.

The low-frequency constraints are weak enough to allow a wide range of attenuation structures. To illustrate the possibilities, LJ23 developed a spatially averaged broadband attenuation model for Southern California consistent

with the low-frequency and high-frequency data. Figure 6 shows the wavenumber and frequency spectra of the total attenuation (solid lines), computed as the sum of a low-frequency intrinsic component (dashed lines) and a high-frequency scattering component (dotted lines). The intrinsic component is modeled as an anelastic absorption band (Minster, 1978) with a peak attenuation of $Q_m^{-1}=1/360$, a low-frequency cutoff at $f_1=0.0001$ Hz, and a high-frequency cutoff at $f_2=0.5$ Hz. The scattering component is the Sato-Fehler model with parameters (4), determined by fitting the spatially averaged frequency spectra of Fig. 3.

The composite model features attenuation peaks centered at wavenumbers slightly less than the scattering peak at $k_{\rm peak}=0.8~{\rm km^{-1}}$, which corresponds to $f_{\rm peak}=0.8~{\rm Hz}$ for P and 0.5 Hz for S. The Q_S^{-1} maximum for Southern California is similar to the attenuation peak first sketched for Japan by Aki in his seminal 1980 paper (Aki, 1980, Figs. 8 and 9), and the location of this peak near 0.5 Hz has been validated in subsequent studies (Sato et al., 2012). The 0.1-1.0 Hz model averages are $Q_S^{-1}\approx 1/200$ and $Q_P^{-1}\approx 1/300$, consistent with the observed low-frequency attenuation. Adding the absorption band accounts for the small (20%) difference in our high-frequency estimates of α_P and α_S , which implies $B_P(k)>B_S(k)$ in the high-frequency band.

The seismic albedos rise from near zero at low wavenumbers to near unity at high wavenumbers (Fig. 6b). Owing to the relative weakness of the anelastic attenuation, both albedos exceed 0.5 at frequencies above about 0.1 Hz. In other words, the broadband model implies that scattering attenuation dominates over intrinsic attenuation even at frequencies less than 1 Hz. The low-frequency albedos are highly uncertain, however. Better estimates are likely to come from the improvements to the wavefield simulations, exemplified in the recent work by Olsen and his colleagues (Withers et al., 2018; Savran and Olsen, 2019; Hu et al., 2022).

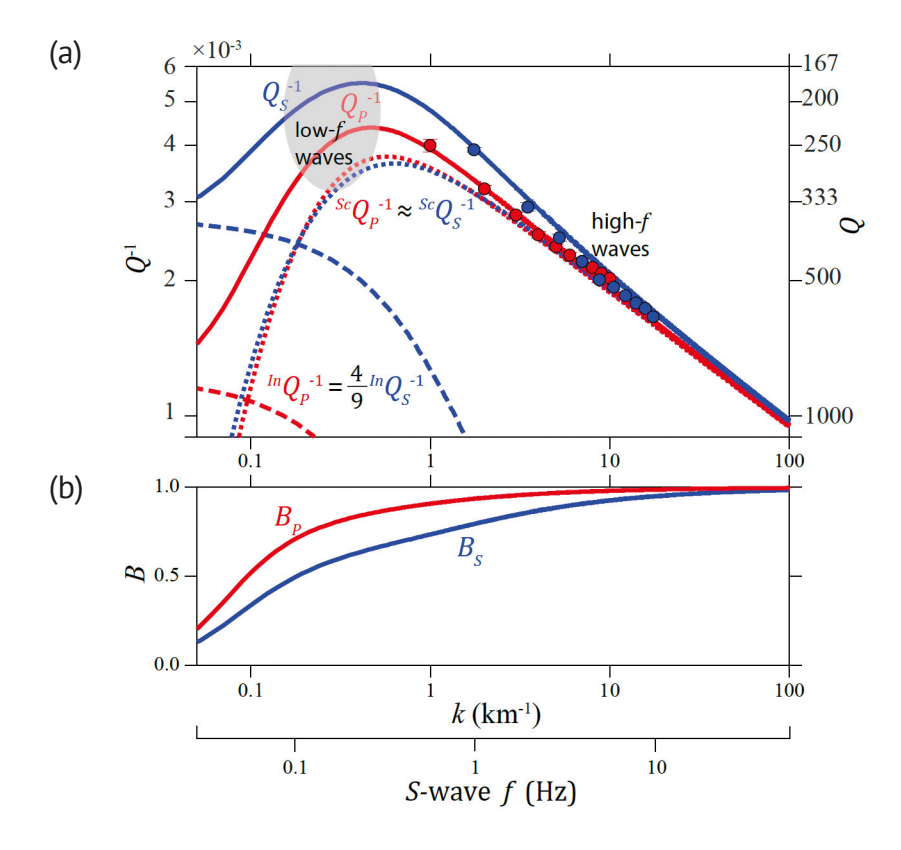


Figure 6. LJ23 broadband attenuation model for Southern California. (a) Comparison of the observed values of Q_P^{-1} (red dots) and Q_S^{-1} (blue dots) with the total attenuation model (solid curves). Data are the spatially averaged values from Fig. 3, plotted against wavenumber $k = 2\pi f/V$ using the scaling velocities $V_P = 6.3$ km/s and $V_S = 3.6$ km/s. The S-wave frequency scale is also shown. Scattering attenuation (dotted curves) is from a Sato-Fehler model with parameters $\varepsilon_0 = 7.5\%$, a = 8 km, v = 0.15, and $\psi_c = 40^\circ$. Intrinsic attenuation (dashed curves) is from an absorption-band model with parameters $Q_m^{-1} = 1/360$, $f_1 = 0.0001$ Hz, $f_2 = 0.5$ Hz, and $Q_P^{-1}/Q_S^{-1} = 4/9$. (b) Seismic albedos B_P and B_S implied by the hypothetical broadband model of panel (a), plotted as a function of wavenumber (Source: LJ23, Fig. 7a).

4. Discussion and conclusions

Velocity and attenuation tomography applied to the abundant datasets of the SCSN reveal a coherent picture of the large-scale tectonic structure and small-scale heterogeneity of the Southern California crust. The tomographic results favor the two main hypotheses, H1 and H2, stated in the Introduction.

4.1 Tectonic regionalization

Cluster analysis of the 1.5 million CVM-S4.26 velocity profiles shows that the large-scale geographic variations in crustal structure can be approximated by a small set ($K \sim 7$) of tectonically coherent regions. The $R7_{\gamma}$ regions (Fig. 1a) have profile averages that display substantial variations in the layer velocities and Moho depths, reflecting regional differences in composition and tectonic evolution (Fig. 1b). Profile variability within the tectonic regions is typically smaller than the profile differences between the regions.

The tomographic regions are multiply connected domains that strongly correlate with well-recognized physiographic and geologic provinces. A prime example is the batholithic terrane of the California Arc, which geologists have separated into an older, western zone of more gabbroic plutons and a younger, eastern zone of more granitic plutons. Two of the $R7_{\gamma}$ tomographic regions, PR and SN, replicate this fundamental dichotomy with remarkable geographic accuracy. PR is geochemically more oceanic and petrologically more mafic, whereas SN is more continental and more felsic.

 $R7_{\gamma}$ separates the sedimentary basins of Southern California into two types, one associated with the Salton Trough (ST) and one with the Great Valley (GV). ST crust is thinner than GV crust and has higher velocities in the lower crust, indicating a more mafic composition. The tomographic regionalization associated the Los Angeles basins with ST and the Santa Maria and Ventura basins with GV, in agreement with geological and geophysical observations.

The regional boundaries at depth align with geologic features at the surface. The dashed lines in Fig. 1a identify thirteen examples where the surface manifestations of the regional boundaries were classified by EJ19 as active faults, inactive faults, topographic fronts, or geochemical transitions (see references in Table 2). The boundary zones between tectonic regions are typically, though not always, localized structures with characteristic widths comparable to a crustal thickness.

We converted the V_P averages to densities using Brocher's (2005) relationship and found that the average crustal columns in Fig. 1b are in approximate isostatic equilibrium; i.e., large mass variations in the upper crust are balanced by equally large variations in the middle and lower crust (Fig. 2). The observation of isostatic balance among the tomographic regions adds to our confidence in the seismic reliability and tectonic credibility of the regionalization. The layer averages and Moho depths of the centroid profiles provide constraints on models of crustal composition and tectonic evolution, as illustrated by the SN \rightarrow MD \rightarrow PT progression from thicker, more felsic crust to thinner, more mafic crust.

Tectonic regionalization (TR) is a structural idealization that approximates the lateral variability within a study area by a mosaic of discrete, disjunct tectonic regions, each characterized by an average lithospheric column. The "TR idealization" is most effective in summarizing structural information where the profile variability within the tectonic regions is small compared to the profile differences among the regions. The efficacy of the $R7_{\gamma}$ tomographic regionalization in representing the subsurface geography of major tectonic units in Southern California indicates that the TR idealization works surprisingly well in this portion of the Pacific-North America plate boundary. It will be interesting to see whether the TR idealization is equally effective in representing large-scale crustal variations in other continental environments.

4.2 Scattering by small-scale heterogeneities

Elastic scattering from small-scale heterogeneities of high fractal dimension appears to be the primary mechanism for the attenuation of high-frequency P and S waves propagating through the upper and middle crust of Southern California. As a function of wavenumber, Q_P^{-1} and Q_S^{-1} are nearly equal and decay at about the same rate – equalities that are signatures of scattering. The amplitude of the scattering varies systematically among the tectonic regions

and roughly correlates with the amount of faulting and distributed deformation within a tectonic region. Tectonic units that are more homogeneous and relatively undeformed, specifically the SN and PR batholithic regions, show lower attenuation than the more strongly deformed parts of the ST, MD, and LA regions (Fig. 4).

S-wave coda studies in Southern California yield higher attenuation factors, larger decay exponents, and lower seismic albedos in the 1-10 Hz band than the broadband attenuation model of Fig. 6 (Jin et al., 1994; Eulenfeld and Wegler, 2017; Wang and Shearer, 2017). Explaining these discrepancies should be a priority for future research on crustal attenuation structure.

The role of elastic scattering in continental regions outside of Southern California also deserves reevaluation. For example, Atkinson and her colleagues have studied high-frequency S-wave attenuation in the stable crust of southeastern Canada and the eastern United States ("eastern North America"). They estimated values of $Q_S^{-1}(1 \text{ Hz})$ ranging from 1/893 to 1/525 and values of α_S ranging from 0.32 to 0.45 (Atkinson, 1989; Atkinson, 2004; Atkinson & Mereu, 1992; Atkinson & Boore, 2014). Their decay exponents are consistent with our estimate of $\alpha_S = 0.37 \pm 0.02$ (Fig. 3). According to the scattering hypothesis, this near equality implies that small-scale heterogeneity decays with wavenumber at about the same rate in eastern North America as it does in Southern California; hence, the lower attenuation factors observed for stable continent crust can be primarily ascribed to a reduction in the RMS amplitude of the heterogeneity, as in Fig. 5. The higher propagation efficiency observed in stable continental regions can thus be explained by a rigid crust that is more homogeneous, as well as colder, than the weaker, deforming crust of Southern California.

The generation of small-scale crustal heterogeneity by regional deformation is a poorly understood process. Fault damage zones certainly contribute to the small-scale heterogeneity around major active faults (Lyakhovsky and Ben-Zion, 2009; Powers and Jordan, 2010; Ben-Zion and Zaliapin, 2019). Detailed mapping of the 2019 Ridgecrest faulting sequence indicates that the damage volumes associated with major earthquakes, as well as the consequent reductions in shear rigidity, may be higher and more widely distributed than previously thought (Rodriguez Padilla et al., 2022). The question remains open, however, as to whether distributed deformation, aseismic as well as seismic, can create the broad zones of high attenuation seen in Fig. 4. High rates of distributed deformation within the regions of high attenuation are indicated by kinematic models constructed to fit fault slip rates and geodetic relative motions. Bird (2009) estimated that, across Southern California, about one-third of the Pacific-North America relative plate motion is accommodated by distributed permanent strain between modeled faults. "Off-fault" deformation fractions of 31-58% have been obtained by kinematic models of the western United States recently developed for use in the National Seismic Hazard Model (Pollitz et al., 2023; Johnson et al., 2023).

While the distributed deformation appears to be substantial, its ability to generate volumetric velocity heterogeneity of sufficient amplitude and high fractal dimension has not yet been demonstrated. One possible mechanism is the interaction between viscous flow and frictional sliding within rheologically inhomogeneous crustal layers. Two-phase models of strain localization in fault zones comprising interconnected viscously weak material surrounding stronger visco-frictional lenses have been developed by Fagereng and Beall (2021). This type of visco-frictional interplay could potentially enhance the heterogeneity and anisotropy within the seismogenic zone. Such a mechanism would produce less heterogeneity in the lower crust, where frictional sliding is inhibited by higher yield strengths and viscous flow is promoted by higher temperatures (Fagereng and Beall, 2021). The smaller attenuation anomalies seen in the lower crust (Fig. 4) are consistent with less heterogeneity.

The transition from anelasticity-dominated attenuation at low frequencies to scattering-dominated attenuation at high frequencies (Fig. 6) may be related to the increase in seismic waveform complexity observed as wavenumbers approach $k_{\rm peak}$. At lower wavenumbers, deterministic solutions to the anelastic wave equation using 3D models such as CVM-S4.26 can reproduce the salient features of the waveforms from small sources, often achieving wiggle-for-wiggle coherence in the main seismic phases (e.g., Lee et al., 2014b). However, the ability to deterministically model waveforms degrades abruptly as the wavenumber approaches $k_{\rm peak}$, so that seismogram synthesis at higher wavenumbers requires stochastic methods to reproduce the wavefield complexity (e.g., Frankel and Clayton, 1986; Savran and Olsen, 2019). This deterministic-stochastic transition is well recognized in ground-motion modeling. For example, it is built into the structure of the SCEC Broadband Platform, which synthesizes seismograms by deterministic simulations at low frequencies and stochastic simulations at high frequencies, and then merges the two spectra in an overlap band of 0.5-1.0 Hz (Goulet et al., 2015; Maechling et al., 2015). According to the scattering hypothesis, the deterministic-stochastic transition marks a rapid decrease in the scattering mean free path as the wavenumber approaches $k_{\rm peak}$.

Acknowledgments. The research summarized in this article was accomplished in collaboration with my students, post-docs, and SCEC colleagues over the last two decades. I especially want to acknowledge the work of Billy Eymold, who carried out the cluster analysis described in Section 2, and Yu-Pin Lin, who conducted the data analysis and attenuation tomography of Section 3. I thank Andrea Morelli and Mike Oskin for their helpful comments on the manuscript. The CVM-S4.26 model can be accessed at https://github.com/SCECcode/ucvmc, and the SCAT model can be accessed at https://github.com/yupinlin/SouthernCaliforniaQmodel. Output files of the regionalizations can be downloaded at https://doi.org/10.5281/zenodo.3525443. The SCEC contribution number for this paper is 13671.

References

- Ajala, R., P. Persaud, J. M. Stock, G. S. Fuis et al. (2019). Three-dimensional basin and fault structure from a detailed seismic velocity model of Coachella Valley, Southern California, J. Geophys. Res. Solid Earth, 124, 4728-4750, doi:10.1029/2018JB016260.
- Aki, K. (1980). Attenuation of shear-waves in the lithosphere for frequencies from 0.05 to 25 Hz, Phys. Earth Planet. Inter., 21, 50-60, doi:10.1016/0031-9201(80)90019-9.
- Aki, K. and P. G. Richards (2002). Quantitative Seismology, 2nd edition, University Science Books, 700 pp, ISBN:978-1-891389-63-4.
- Allam, A. A. and Y. Ben-Zion (2012). Seismic velocity structures in the southern California plate-boundary environment from double-difference tomography, Geophys. J. Int., 190, 1181-1196, doi:10.1111/j.1365-246X.2012.05544.x.
- Arthur, D. and S. Vassilvitskii (2007). *K*-means++: The advantages of careful seeding. In Proceedings of the Eighteenth Annual ACM-SIAM Symposium on Discrete Algorithms, Society for Industrial and Applied Mathematics, pp. 1027-1035.
- Atkinson, G. M. (1995). Attenuation and source parameters of earthquakes in the Cascadia region, Bull. Seismol. Soc. Am., 85, 1327-1342, doi:10.1785/BSSA0850051327.
- Atkinson, G. M. (1989). Attenuation of the Lg phase and site response for the Eastern Canada Telemetered Network, Seism. Res. Lett., 60, 59-69, doi:10.1785/gssrl.60.2.59.
- Atkinson, G. M. (2004). Empirical attenuation of ground-motion spectral amplitudes in southeastern Canada and the northeastern United States, Bull. Seismol. Soc. Am., 94, 1079-1095, doi:10.1785/0120030175.
- Atkinson, G. M. and R. Mereu (1992). The shape of ground motion attenuation curves in southeastern Canada, Bull. Seismol. Soc. Am., 82, 2014-2031, doi:10.1785/BSSA0820052014.
- Atkinson, G. M. and D. Boore (2014). The attenuation of Fourier amplitudes for rock sites in eastern North America, Bull. Seismol. Soc. Am., 104, 513-528, doi:10.1785/0120130136.
- Beard, S., G. B. Haxel, R. J. Dorsey, K. A. McDougall et al. (2016). Late Neogene deformation of the Chocolate Mountains Anticlinorium: Implications for deposition of the Bouse Formation and early evolution of the Lower Colorado River, 30th Annual Desert Symposium, 176-184, http://pubs.er.usgs.gov/publication/70169150.
- Benson, P. M., P. G. Meredith and A. Schubnel (2006). Role of void space geometry in permeability evolution in crustal rocks at elevated pressure, J. Geophys. Res. Solid Earth, 111, B12203, doi:10.1029/2006JB004309.
- Ben-Zion, Y. and I. Zaliapin (2019). Spatial variations of rock damage production by earthquakes in southern California, Earth Planet. Sci. Lett., 512, 84-193, doi:10.1016/j.epsl.2019.02.006.
- Bird, P. (2009). Long-term fault slip rates, distributed deformation rates, and forecast of seismicity in the western United States from joint fitting of community geologic, geodetic, and stress direction data sets, J. Geophys. Res. Solid Earth, 114, B11403, doi:10.1029/2009JB006317.
- Brocher, T. M. (2005). Empirical relations between elastic wavespeeds and density in the Earth's crust, Bull. Seismol. Soc. Am., 95, 2081-2092, doi:10.1785/0120050077.
- Chapman, A. D., J. B. Saleeby, D. J. Wood, A. Piasecki et al. (2012). Late Cretaceous gravitational collapse of the southern Sierra Nevada batholith, California, Geosphere, 8, 314-341, doi:10.1130/GES00740.1.
- Chapman, A. D., C. E. Jacobson, W. G. Ernst, M. Grove et al. (2016). Assembling the world's type shallow subduction complex: Detrital zircon geochronologic constraints on the origin of the Nacimiento block, central California Coast Ranges, Geosphere, 12, 533-557, doi:10.1130/GES01257.1.
- Chen, P., T. H. Jordan and L. Zhao (2007a). Full three-dimensional waveform tomography: a comparison between the scattering-integral and adjoint-wavefield methods, Geophys. J. Int., 170, 175-181, doi: 10.1111/j.1365-246x.2007.03429.x.

- Chen, P., L. Zhao and T. H. Jordan (2007b). Full 3D tomography for the crustal structure of the Los Angeles region, Bull. Seismol. Soc. Am., 97, 1094-1120, doi:10.1785/0120060222.
- Condie, K. C. (1982). Plate-tectonics model for Proterozoic continental accretion in the southwestern United States, Geology, 10, 37-42, doi:10.1130/0091-7613(1982)10<37:PMFPCA>2.0.CO;2.
- Christensen, N. I. and W. D. Mooney (1995). Seismic velocity structure and composition of the continental crust: a global view, J. Geophys. Res. Solid Earth, 100, 9761-9788, doi:10.1029/95JB00259.
- Dolan, S., C. Bean and B. Riollet (1998). The broad-band fractal nature of heterogeneity in the upper crust from petrophysical logs, Geophys. J. Int., 132, 489-507, doi:10.1046/j.1365-246X.1998.00410.x.
- Ehlig, P. (1979). The Late Cenozoic evolution of the Capistrano Embayment. In: Fife, D. L. (ed.), Geology Guide to San Onofre Nuclear Station and Adjacent Regions of Southern California, Pacific Sections. American Association of Petroleum Geologists, SEPM, and Society of Exploration Geophysicists, pp. A38-A46.
- Eulenfeld, T. and U. Wegler (2017). Crustal intrinsic and scattering attenuation of high-frequency shear waves in the contiguous United States, J. Geophys. Res. Solid Earth, 122, 4676-4690. doi:10.1002/2017JB014038.
- Eymold, W. K. and T. H. Jordan (2019). Tectonic regionalization of the Southern California crust from tomographic cluster analysis, J. Geophys. Res. Solid Earth, 124, 11,840-11,865, doi:10.1029/2019JB018423.
- Fagereng, Å. and A. Beall (2021). Is complex fault zone behaviour a reflection of rheological heterogeneity?, Philos. Trans. R. Soc., A379, 20190421, doi:10.1098/rsta.2019.0421.
- Fang, H., M. C. A. White, Y. Lu and Y. Ben-Zion (2022). Seismic traveltime tomography of Southern California using Poisson-Voronoi cells and 20 years of data, J. Geophys. Res. Solid Earth, 127, e2021JB023307, doi:10.1029/2021JB023307.
- Frankel, A. (1991). Mechanisms of seismic attenuation in the crust: Scattering and anelasticity in New York state, South Africa, and southern California, J. Geophys. Res. Solid Earth, 96, 6269-6289, doi:10.1029/91JB00192.
- Frankel, A. and R. W. Clayton (1986). Finite difference simulations of seismic scattering: implications for the propagation of short-period seismic waves in the crust and models of crustal heterogeneity, J. Geophys. Res. Solid Earth, 91, 6465-6489, doi:10.1029/JB091iB06p06465.
- Fuis, G. S., T. Ryberg, W. J. Lutter and P. L. Ehlig (2001). Seismic mapping of shallow fault zones in the San Gabriel Mountains from the Los Angeles Region Seismic Experiment, southern California, J. Geophys. Res. Solid Earth, 106, 6549-6568.
- Gans, P. B., and W. A. Bohrson (1998). Suppression of volcanism during rapid extension in the Basin and Range Province, United States, Science, 279, 66-68, doi:10.1126/science.279.5347.66.
- Godfrey, N. J. and S. L. Klemperer (1998). Ophiolitic basement to a forearc basin and implications for continental growth: The Coast Range/Great Valley ophiolite, California, Tectonics, 17, 558-570.
- Godfrey, N. J., G. S. Fuis, V. Langenheim, D. A. Okaya & T. M. Brocher (2002). Lower crustal deformation beneath the central Transverse Ranges, southern California: Results from the Los Angeles Region Seismic Experiment, J. Geophys. Res. Solid Earth, 107, B7, 2144, doi:10.1029/2001JB000354.
- Goulet, C. A., N. A. Abrahamson, P. G. Somerville and K. E. Wooddell (2015). The SCEC broadband platform validation exercise; methodology for code validation in the context of seismic-hazard analyses, Seismol. Res. Lett., 86, 17-26, doi:10.1785/0220140104.
- Graves, R. W., B. T. Aagaard, K. W. Hudnut, L. M. Star et al. (2008). Broadband simulations for $M_{\rm w}$ 7.8 southern San Andreas earthquakes: Ground motion sensitivity to rupture speed, Geophys. Res. Lett., 35, L22302, doi:10.1029/2008GL035750.
- Hauksson, E. (2000). Crustal structure and seismicity distribution adjacent to the Pacific and North America plate boundary in southern California, J. Geophys. Res. Solid Earth, 105, 13875, doi:10.1029/2000JB900016.
- Hauksson, E., P. Small, K. Hafner, R. Busby et al. (2001). Southern California Seismic Network: Caltech/USGS Element of TriNet 1997-2001, Seismol. Res. Lett., 72, 690-704, doi:10.1785/gssrl.72.6.690.
- Hauksson, E. and P. M. Shearer (2006). Attenuation models (Q_P and Q_S) in three dimensions of the southern California crust: Inferred fluid saturation at seismogenic depths, J. Geophys. Res. Solid Earth, 111, B05302, doi: 10.1029/2005JB003947.
- Hearn, T. M. (2020). Crustal attenuation from USArray ML amplitude tomography, Geophys. J. Int., 224, 199-206, doi:10.1093/gji/ggaa445.
- Howard, K. A., P. K. House, R. J. Dorsey and P. A. Pearthree (2015). River-evolution and tectonic implications of a major Pliocene aggradation on the lower Colorado River: the Bullhead Alluvium, Geosphere, 11, 1-30, doi:10.1130/GES01059.1.

- Hu, Z., K. B. Olsen and S. M. Day (2022). 0-5 Hz deterministic 3-D ground motion simulations for the 2014 La Habra, California, Earthquake, Geophys. J. Int., 230, 2162-2182., doi:10.1093/gji/ggac174.
- Hubbard, J., Shaw, J. H. Dolan, J. Pratt et al. (2014). Structure and seismic hazard of the Ventura Avenue Anticline and Ventura Fault, California: Prospect for large, multisegment ruptures in the western Transverse Ranges, Bull. Seismol. Soc. Am., 104, 1070-1087, doi:10.1785/0120130125.
- Jiang, H. and C. T. A. Lee (2017). Coupled magmatism-erosion in continental arcs: Reconstructing the history of the Cretaceous Peninsular Ranges batholith, southern California through detrital hornblende barometry in forearc sediments, Earth Planet. Sci. Lett., 472, 69-81, doi:10.1016/j.epsl.2017.05.009
- Jin, A., K. Mayeda, D. Adams and K. Aki (1994). Separation of intrinsic and scattering attenuation in southern California using TERRAscope data, J. Geophys. Res. Solid Earth, 99, 17,835-17,848, doi:10.1029/94JB01468.
- Johnson, K. M., W. C. Hammond and R. J. Weldon (2023). Review of geodetic and geologic deformation models for 2023 US National Seismic Hazard Model, Seismol. Res. Lett., 114, 1407-1436, doi: 10.1785/0220230137.
- Jordan, T. H. (1979). Mineralogies, densities and seismic velocities of garnet lherzolites and their geophysical implications, in The Mantle Sample: Inclusions in Kimberlites and Other Volcanics, ed. by F.R. Boyd and H.O.A. Meyer, American Geophysical Union, Washington, D.C., pp. 1-14, doi:10.1029/SP016p0001.
- Kaban, M. K. and W. D. Mooney (2001). Density structure of the lithosphere in the southwestern United States and its tectonic significance, J. Geophys. Res. Solid Earth, 106, 721-739, doi:10.1029/2000JB900235.
- Kawahara, J. (2002). Cutoff scattering angles for random acoustic media, J. Geophys. Res. Solid Earth, 107, doi:10.1029/2001JB000429.
- Kistler, R. W. and Z. E. Peterman (1978). Reconstruction of crustal blocks of California on the basis of initial strontium isotopic compositions of Mesozoic granitic rocks, U.S. Geol. Surv. Prof. Paper 1071, 17 pp.
- Klotsko, S., N. Driscoll, G. Kent and D. Brothers (2015). Continental shelf morphology and stratigraphy offshore San Onofre, California: The interplay between rates of eustatic change and sediment supply, Marine Geology, 369, 116-126, doi:10.1016/j.margeo.2015.08.003.
- Knopoff, L. (1964). Q, Reviews of Geophysics, 2, 625-660, doi:10.1029/RG002i004p00625.
- Kucks, R. P. (1999). Bouguer gravity anomaly data grid for the conterminous US, U.S. Geological Survey Digital Data Series DDS-9, https://mrdata.usgs.gov/services/gravity?request=getcapabilities&service=WMS&version=1.3.
- Lachenbruch, A. H., J. H. Sass and P. Morgan (1994). Thermal regime of the southern Basin and Range Province: 2. Implications of heat flow for regional extension and metamorphic core complexes, J. Geophys. Res. Solid Earth, 99, 22121-22133, doi:10.1029/94JB01890.
- Langenheim, V. E., R. C. Jachens, D. M. Morton, R. W. Kistler et al. (2004). Geophysical and isotopic mapping of preexisting crustal structures that influenced the location and development of the San Jacinto fault zone, southern California, Geol. Soc. Am. Bull., 116, 1143-1157, doi:10.1130/B25277.1.
- Lee, E.-J., P. Chen, T. H. Jordan, P. B. Maechling et al. (2014a). Full-3D tomography for crustal structure in Southern California based on the scattering-integral and the adjoint-wavefield methods, J. Geophys. Res. Solid Earth, 119, 6421-6451, doi:10.1002/2014JB011346.
- Lee, E.-J., P. Chen and T. H. Jordan (2014b). Testing waveform predictions of 3D velocity models against two recent Los Angeles earthquakes, Seismol. Res. Lett., 85, 1275-1284.
- Lee, E.-J. and P. Chen (2016). Improved basin structures in Southern California obtained through full-3D seismic waveform tomography (F3DT), Seismol. Res. Lett., 87, 874-881, doi:10.1785/0220160013.
- Lee, E.-J. and P. Chen (2017). Subsurface fault geometries in Southern California illuminated through full-3D seismic waveform tomography (F3DT), Tectonophysics, 703-704, 42-49, doi:10.1016/j.tecto.2017.03.005.
- Lin, G., C. H. Thurber, H. Zhang, E. Hauksson et al. (2010). A California statewide three-dimensional seismic velocity model from both absolute and differential times, Bull. Seismol. Soc. Am., 100, 225-240, doi:10.1785/0120090028.
- Lin, Y.-P. and T. H. Jordan (2018). Frequency-dependent attenuation of P and S waves in Southern California, J. Geophys. Res. Solid Earth, 123, 5814-5830, doi:10.1029/2018JB015448.
- Lin, Y. P. and T. H. Jordan (2023). Elastic scattering dominates high-frequency seismic attenuation in southern California, Earth Planet. Sci. Lett., 616, 118227, doi:10.1016/j.epsl.2023.118227.
- Lu, Y. and Y. Ben-Zion (2022). Validation of seismic velocity models in southern California with full-waveform simulations, Geophys. J. Int., 229, 1232-1254, doi:10.1093/gji/ggab534.
- Luffi, P., J. B. Saleeby, C.-T. A. Lee and M. N. Ducea (2009). Lithospheric mantle duplex beneath the central Mojave Desert revealed by xenoliths from Dish Hill, California, J. Geophys. Res. Solid Earth, 114, B03202, doi:10.1029/2008JB005906.

- Lyakhovsky, V. and T. Ben-Zion (2009). Evolving geometrical and material properties of fault zones in a damage rheology model, Geochem. Geophys. Geosyst., 10, Q11011, doi:10.1029/2009GC002543.
- Maechling, P. J., F. Silva, S. Callaghan and T. H. Jordan (2015). SCEC Broadband Platform: System Architecture and Software Implementation, Seismol. Res. Lett., 86, 27-38, doi:10.1785/0220140125.
- Marshall, S. T., G. J. Funning, H. E. Krueger, S. E. Owen and J. P. Loveless (2017), Mechanical models favor a ramp geometry for the Ventura-Pitas Point fault, California, Geophys. Res. Lett., 44, 1311-1319, doi:10.1002/2016GL072289.
- Mason, C. C., J. A. Spotila, G. Axen, R. J. Dorsey et al. (2017). Two-phase exhumation of the Santa Rosa Mountains: Low- and high-angle normal faulting during initiation and evolution of the southern San Andreas Fault system, Tectonics, 36, 2863-2881, doi:10.1002/2017TC004498.
- Mayo, D. G. (2018). Statistical inference as severe testing: How to get beyond the statistics wars, Cambridge University Press, 486 pp.
- Miller, J. S., A. F. Glazner, G. L. Farmer, I. B. Suayah et al. (2000). A Sr, Nd, and Pb isotopic study of mantle domains and crustal structure from Miocene volcanic rocks in the Mojave Desert, California, Geol. Soc. Am. Bull., 112, 1264-1279.
- Minster, J. B. (1978). Transient and impulse responses of a one-dimensional linearly attenuating medium II. A parametric study, Geophys. J. R. Astron. Soc., 52, 503-524, doi:10.1111/j.1365-246X.1978.tb04246.x.
- Nakata, N. and G. C. Beroza (2015). Stochastic characterization of mesoscale seismic velocity heterogeneity in Long Beach, California, Geophys. J. Int., 203, 2049-2054, doi:10.1093/gji/ggv421.
- Nelson, K. D., T. F. Zhu, A. Gibbs, R. Harris et al. (1986). COCORP deep seismic reflection profiling in the northern Sierra Nevada, California, Tectonics, 5, 321-333, doi:10.1785/BSSA0890040888.
- Olsen, K. B., S. M. Day and C. R. Bradley (2003). Estimation of Q for long-period (> 2 sec) waves in the Los Angeles basin, Bull. Seismol. Soc. Am., 93, 627-638, doi:10.1785/0120020135.
- Parsons, T. (2006). Chapter 7, The basin and range province, in Olsen, K. H (ed.), Developments in Geotectonics, 25, 277-326, doi:10.1016/S0419-0254(06)80015-7.
- Pei, S. and Y. J. Chen (2010). The updated crustal attenuation in north China using ML amplitude tomography, Earthquake Science, 23, 541-548, doi:10.1007/s11589-010-0753-3.
- Phillips, W. S. and R. J. Stead (2008). Attenuation of Lg in the western US using the US Array. Geophys. Res. Lett., 35, L07307, doi:10.1029/2007GL032926
- Pollitz, F. F. (2022). Viscoelastic fault-based model of crustal deformation for the 2023 update to the US National Seismic Hazard model, Seismol. Res. Lett., 93, 3087-3099, doi:10.1785/0220220137.
- Powers, P. and T. H. Jordan (2010). Seismicity distribution across strike-slip faults in California, J. Geophys. Res. Solid Earth, 115, B05305, doi:10.1029/2008JB006234.
- Pullammanappallil, S., A. R. Levander and S. P. Larkin (1997). Estimation of crustal stochastic parameters from seismic exploration data, J. Geophys. Res. Solid Earth, 102, 15269-15286, doi:10.1029/97JB01144.
- Raoof, M., R. B. Herrmann and L. Malagnini (1999). Attenuation and excitation of three-component ground motion in southern California, Bull. Seismol. Soc. Am., 89, 888-902, doi:10.1785/BSSA0890040888.
- Rodriguez Padilla, A. M., M. E. Oskin, C. W. D. Milliner and A. Plesch (2022). Accrual of widespread rock damage from the 2019 Ridgecrest earthquakes, Nat. Geosci., 15, 222-226, doi:10.1038/s41561-021-00888-w.
- Romanyuk, T., W. D. Mooney and S. Detweiler (2007). Two lithospheric profiles across southern California derived from gravity and seismic data, J. Geodynamics, 43, 274-307.
- Saleeby, J. (2011). Geochemical mapping of the Kings-Kaweah ophiolite belt, California Evidence for progressive mélange formation in a large offset transform-subduction initiation environment, in Wakabayashi, J., & Dilek, Y., eds., Mélanges: Processes of Formation and Societal Significance, Geol. Soc. Am. Special Paper, 480, 31-73, doi:10.1130/2011.2480(02).
- Saleeby, J., L. Le Pourhiet, Z. Saleeby and M. Gurnis (2012). Epeirogenic transients related to mantle lithosphere removal in the southern Sierra Nevada region, California, part I: Implications of thermomechanical modeling, Geosphere, 8, 1286-1309, doi:10.1130/GES00746.1.
- Sass, J. H., A. H. Lachenbruch, S. P. Galanis, P. Morgan et al. (1994). Thermal regime of the southern Basin and Range Province: 1. Heat flow data from Arizona and the Mojave Desert of California and Nevada, J. Geophys. Res. Solid Earth, 99, 22093-22119, doi:10.1029/94JB01891.
- Sato, H., M. Fehler and T. Maeda (2012). Seismic Wave Propagation and Scattering in the Heterogeneous Earth, 2nd ed., Springer, Berlin/Heidelberg, 308 pp.

- Savran, W. and K. Olsen (2016). Model for small-scale crustal heterogeneity in Los Angeles basin based on inversion of sonic log data, Geophys. J. Int., 205, 856-863, doi.:10.1093/gjj/ggw050.
- Savran, W. H. and K. B. Olsen (2019). Ground motion simulation and validation of the 2008 Chino Hills earthquake in scattering media, Geophys. J. Int., 219, 1836-1850 doi:10.1093/gji/ggz399.
- Scheirer, D. S. and R. W. Hobbs (1990). Seismic attenuation in the continental crust SW of England. Geophys. J. Int., 103, 533-540, doi:10.1111/j.1365-246X.1990.tb01789.x.
- Schlotterbeck, B. A. and G. A. Abers (2001). Three-dimensional attenuation variations in Southern California, J. Geophys. Res. Solid Earth, 106, 30,719-30,735.
- Schmandt, B., F.-C. Lin and K. E. Karlstrom (2015). Distinct crustal isostasy trends east and west of the Rocky Mountain Front, Geophys. Res. Lett., 42, 10,290-10,298, doi:10.1002/2015GL066593.
- Shaw, J. H., A. Plesch, C. Tape, M. P. Suess et al. (2015). Unified structural representation of the Southern California crust and upper mantle. Earth Planet. Sci. Lett., 415, 1-15, doi:10.1016/j.epsl.2015.01.016.
- Spotila, J. A. and K. Sieh (2000). Architecture of transpressional thrust faulting in the San Bernardino Mountains, southern California, from deformation of a deeply weathered surface, Tectonics, 19, 589-615, doi:10.1029/1999TC001150.
- Stevens, C. H. and P. Stone (2005). Interpretation of the Last Chance thrust, Death Valley region, California, as an Early Permian décollement in a previously undeformed shale basin, Earth-Sci. Rev., 73, 79-101, doi:10.1016/j. earscirev.2005.04.005.
- Taborda, R., S. Azizzadeh-Roodpish, N. Khoshnevis and K. Cheng (2016). Evaluation of the southern California seismic velocity models through simulation of recorded events, Geophys. J. Int., 205, 1342-1364, doi:10.1093/gji/ggw085.
- Tape, C., Q. Liu, A. Maggi and J. Tromp (2010). Seismic tomography of the southern California crust based on spectral-element and adjoint methods, Geophys. J. Int., 180, 433-462, doi:10.1111/j.1365-246X.2009.04429.x.
- Toksöz, M. N., D. H. Johnston and A. Timur (1979). Attenuation of seismic waves in dry and saturated rocks: I. Laboratory measurements, Geophysics, 44, 681-690, doi:10.1190/1.1440969.
- Tromp, J., C. Tape and Q. Liu (2005). Seismic tomography, adjoint methods, time reversal and banana-doughnut kernels, Geophys. J. Int., 160, 195-216, doi:10.1111/j.1365-246X.2004.02453.x.
- Wang, W. and P. M. Shearer (2017). Using direct and coda wave envelopes to resolve the scattering and intrinsic attenuation structure of Southern California, J. Geophys. Res. Solid Earth, 122, 7236-7251, doi:10.1002/2016JB013810.
- Wang, W. and P. M. Shearer (2019). An improved method to determine coda-Q, earthquake magnitude, and site amplification: Theory and application to southern California, J. Geophys. Res. Solid Earth, 124, 578-598, doi:10.1029/2018JB015961.
- Withers, K. B., K. B. Olsen, S. M. Day and Z. Shi (2018). Ground motion and intraevent variability from 3D deterministic broadband (0-7.5 Hz) simulations along a nonplanar strike-slip fault, Bull. Seismol. Soc. Am., 109, 229-250, doi:10.1785/0120180006.
- Winkler, K. W. and A. Nur (1982). Seismic attenuation: Effects of pore fluids and frictional-sliding, Geophysics, 47, 1-15, doi:10.1190/1.1441276.
- Withers, K. B., K. B. Olsen, S. M. Day and Z. Shi (2018). Ground motion and intra-event variability from 3-D deterministic broadband (0-7.5 Hz) simulations along a non-planar strike-slip fault, Bull. Seism. Soc. Am., 109, 229-250, doi:10.1785/0120180006.
- Yan, Z. and R. W. Clayton (2007). Regional mapping of the crustal structure in southern California from receiver functions, J. Geophys. Res. Solid Earth, 112, B05311, doi:10.1029/2006JB004622.
- Zigone, D., Y. Ben-Zion, M. Campillo and P. Roux (2015). Seismic tomography of the Southern California plate boundary region from noise-based Rayleigh and love waves, Pure Appl. Geophys., 172, 1007-1032, doi:10.1007/s00024-014-0872-1.
- Zhao, L., T. H. Jordan, K. B. Olsen and P. Chen (2005), Fréchet kernels for imaging regional Earth structure based on three-dimensional reference models, Bull. Seismol. Soc. Am., 95, 2066-2080, doi:10.1785/0120050081.